Supporting Information for

Magnetic and Optical Bistability Driven by Thermally- and Photo-Induced Intramolecular Electron Transfer in a Molecular Cobalt-Iron Prussian Blue Analogue

Dongfeng Li,[1] Rodolphe Clérac,[2]* Olivier Roubeau,[2] Etienne Harté,[2] Corine Mathonière,[3]* Rémy Le Bris,[3] and Stephen M. Holmes[1]*

[1]*Department of Chemistry, University of Kentucky, Lexington, Kentucky 40506-0055, USA*

[2]*Université Bordeaux 1; CNRS, Centre de Recherche Paul Pascal - UPR8641, 115 avenue du Dr. A. Schweitzer, 33600 Pessac, France*

[3] *Université Bordeaux 1; CNRS, Institut de Chimie de la Matière Condensée de Bordeaux, UPR9048, 87 avenue du Dr. A. Schweitzer, 33608 Pessac, France*

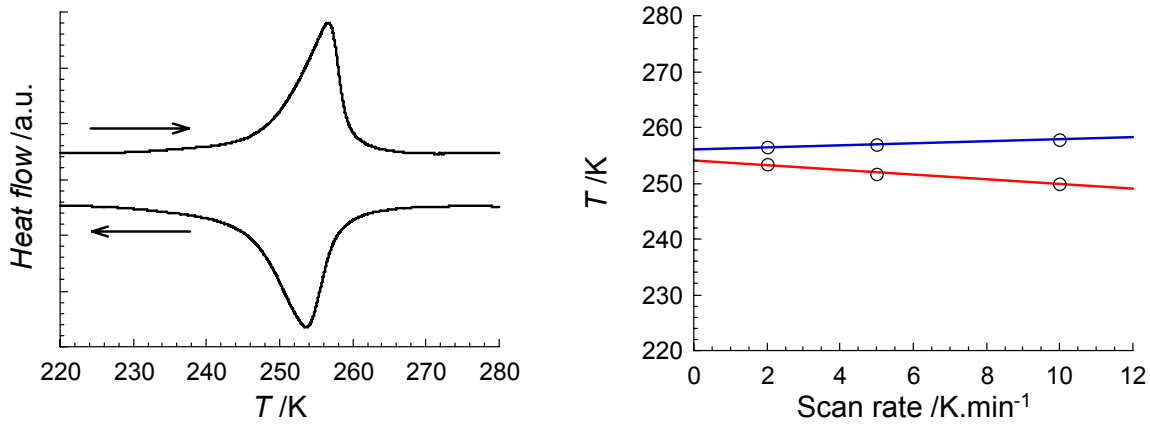

Figure S1. Left: DSC thermograms at a 2 K min^{-1} scan rate for **1** (endothermic peaks are pointing up) **Right:** Evolution of DSC peak temperature vs scan rate emphasizing tiny hysteresis effect (*ca.* 2 K) near transition temperature (255 K). These results are in agreement with magnetic measurements suggesting negligible thermal hysteresis behavior.

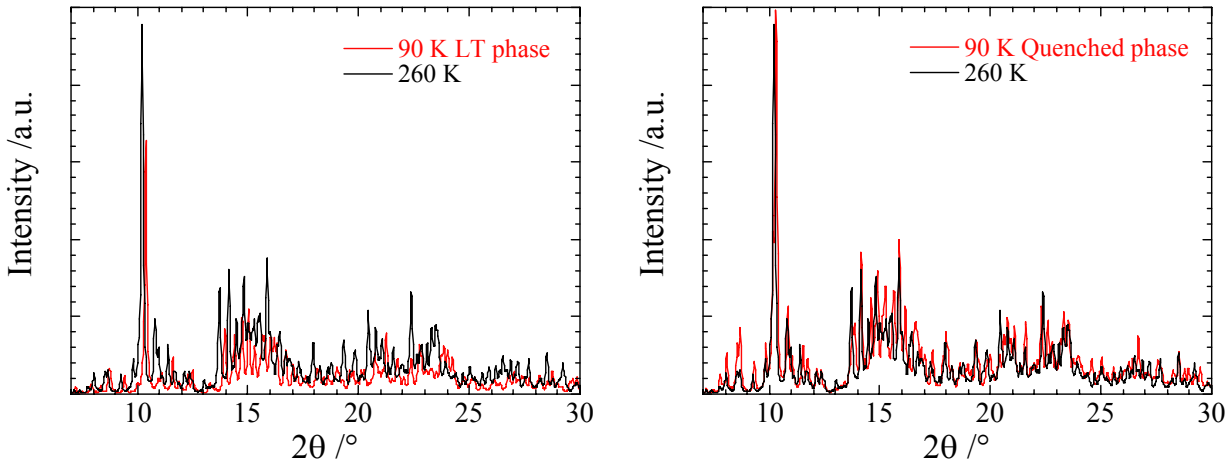

Figure S2. (**left**) Simulated X-ray powder patterns of **1** using the single crystal X-ray data collected at 260 K and 90 K (slowly cooled low temperature, LT, phase). Note: Comparing the 260 K and 90 K LT phase emphasize the *differences* between the two (left). (**right**) Simulated X-ray powder patterns for the 90 K (rapidly cooled, quenched Q, phase) and high temperature (HT phase, 260 K) data collected for **1** Note: Comparing the 260 K and 90 K quenched phases emphasize the *similarities* of both (right).

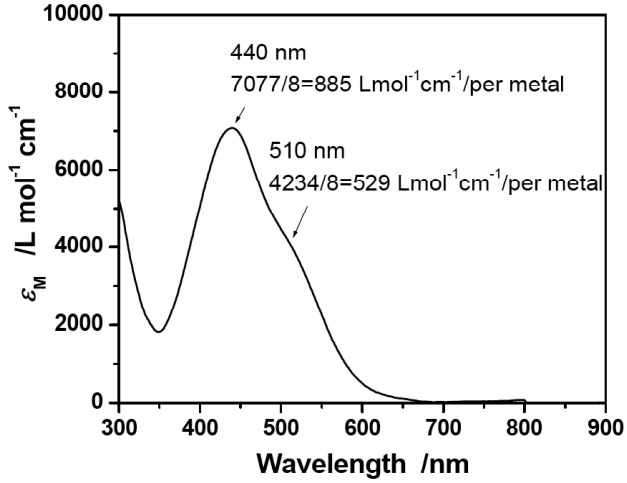

Figure S3. Room temperature UV-vis solution spectrum of **1** in CH_3CN [C = 8.58x10^{-5} M].

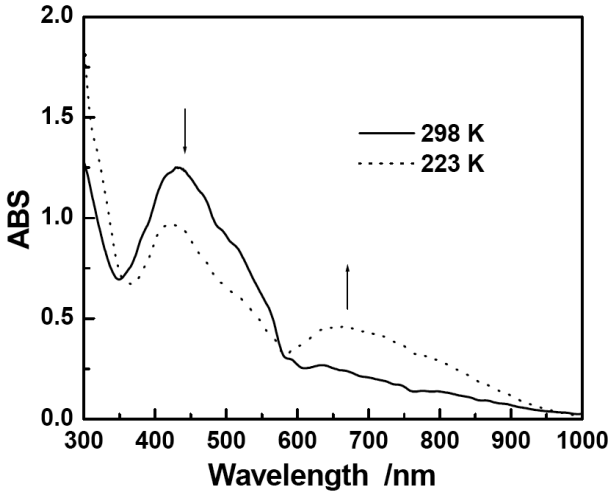

Figure S4. Solid state UV-vis spectra of **1** at 298 (—) and 223 K (···). Note: spectra collected as Nujol mulls between KBr plates.

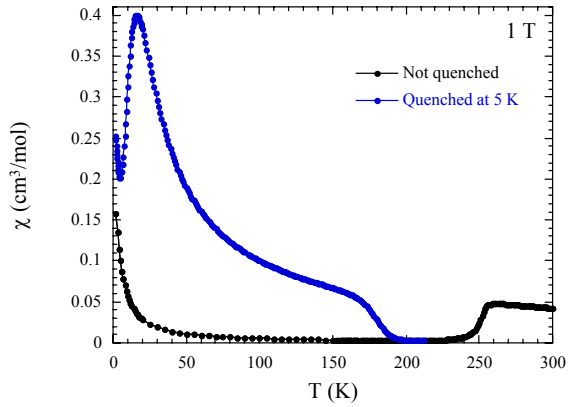

Figure S5. χ vs T data obtained (where $\chi = M/H$) when temperature is altered at rate of 0.4 K min^{-1} for **1** between 1.8 and 300 K (H_{dc} = 1 T) before (•) and after (•) rapid thermal quenching from 300 to 5 K. The lines are guides for the eye.

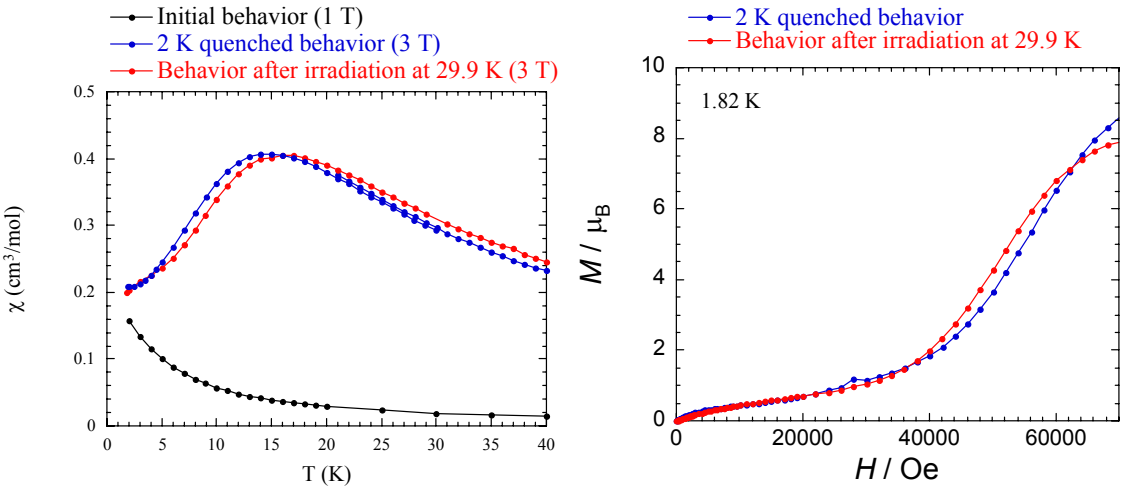

Figure S6. Left: χ vs T data for **1** between 1.8 and 40 K and **Right:** M vs H data at 1.82 K (•) before irradiation or quench, (•) after halogen white light irradiation [575(40) mW cm^{-2}] at 30 K over 20 h, and (•) after a thermal quench (300 → 2 K). The lines are guides for the eye. Note the similarity between the photo-induced and quenched states.

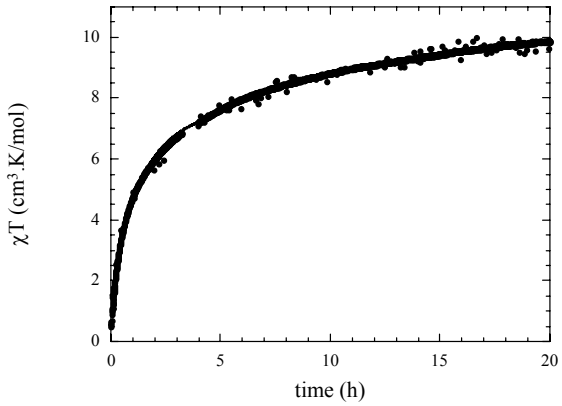

Figure S7. χT vs *time* data obtained for **1** at 30 K (H_{dc} =1 T) at an incident halogen white light power of 575(40) mW cm^{-2}.

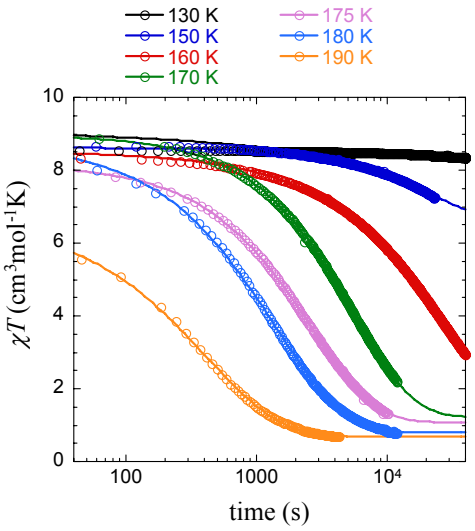

Figure S8. χT vs *time* data obtained for thermally quenched samples (300 → 100 K) of **1** at an applied static magnetic field of H_{dc} = 1 T. The relaxation times were deduced from the fitting the data using a stretched exponential law (solid lines).

Synthesis of $[NEt_4]_2[(pzTp)Fe^{II}(CN)_3]$. Treatment of $[(pzTp)_2Fe^{II}]$ (1.228 g, 2.00 mmol) (pzTp = tetra(pyrazolyl)borate) with $[NEt_4]CN$ (0.967 g, 6.20 mmol) in MeCN (40 ml) for 1 h at 50 °C afforded an orange solution that was evacuated to dryness. The orange residue was dissolved into MeCN (15 mL), filtered, and the filtrate was layered with Et_2O (40 mL). Orange blocks were obtained after 3 d and were isolated via filtration, washed with Et_2O (2 × 5 mL), and dried under vacuum for 2 h. Yield: 1.22 g (86.0 %). Anal Calcd. For $C_{31}H_{52}N_{13}BFe$: C, 55.23; H, 7.80; N, 27.02 . Found: C, 56.14; H, 8.41; N, 28.49. IR (Nujol, cm^{-1}): 3658 (w), 3351 (vs, br), 3240 (vs, br) 3089 (s), 2954 (vs), 2924 (vs), 2855 (vs), 2069 (vs), 2050 (vs), 1499 (vs), 1481 (vs), 1461 (vs), 1411 (vs), 1390 (vs), 1293 (vs), 1213 (vs), 1189 (s), 1174 (s), 1091 (vs), 1056 (s), 1047 (s), 1004 (s), 920 (m), 871 (m), 842 (s), 814 (s), 795 (vs), 780 (vs), 759 (vs), 669 (s), 623 (s). μ_{eff} (μ_B) = 0.

Table S1. Crystallographic data for $[NEt_4]_2[(pzTp)Fe^{II}(CN)_3]\cdot 2H_2O$.

crystal color	brick red
formula	$C_{31}H_{56}BFeN_{13}O_2$
formula wt	709.55
crystal system	Orthorhombic
space group	$P2_12_12_1$
wavelength, λ	0.71073
Temperature, K	90.0(2)
a, Å	14.6607(4)
b, Å	15.5088(4)
c, Å	16.0048(5)
α, º	90.0
β, º	90.0
γ, º	90.0
V, $Å^3$	3639.0(2)
D_c, g cm^{-3}	1.295
Z	4
μ, mm^{-1}	0.463
R_1[a]	0.0573
wR_2[a]	0.1010

[a] $I > 2\sigma(I)$, $R = \sum||F_o| - |F_o||\sum|F_o|$. $R_w = [(\sum w(|F_o| - |F_o|)^2/\sum wF_o^2)]^{1/2}$

Table S2. Selected Bond Distances (Å) and Angles (°) for $[NEt_4]_2[(pzTp)Fe^{II}(CN)_3]\cdot 2H_2O$.

Fe1-C13	1.901(5)	C13-Fe1-C14	88.2(2)
Fe1-C14	1.908(5)	C13-Fe1-C15	88.6(2)
Fe1-C15	1.901(5)	C14-Fe1-C15	90.5(2)
Fe1-N1	2.023(4)	C13-Fe1-N1	90.3(2)
Fe1-N3	1.995(4)	N1-Fe1-N3	86.0(2)
Fe1-N5	1.981(3)	N1-Fe1-N5	87.2(2)

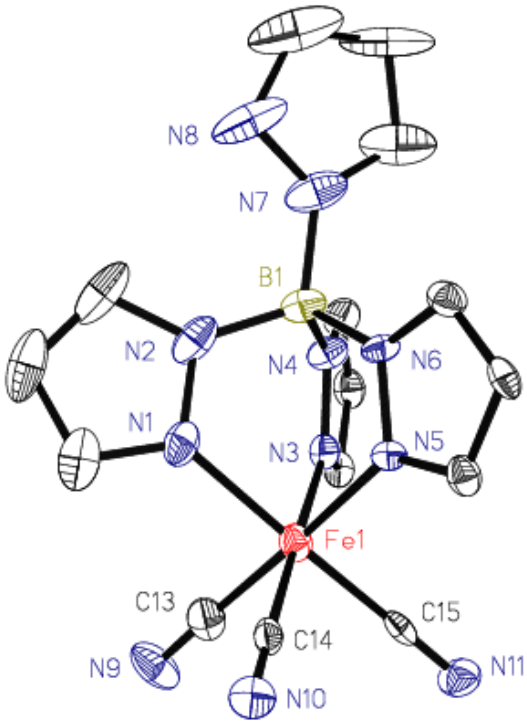

Figure S9. X-ray structure of $[NEt_4]_2[(pzTp)Fe^{II}(CN)_3]\cdot 2H_2O$. Thermal ellipsoids are at the 50% probability level and all cations, lattice solvent, and hydrogen atoms have been eliminated for clarity.